Supporting Information for the manuscript

Antenna-Enhanced Fluorescence Correlation Spectroscopy Resolves Calcium-Mediated Lipid-Lipid-Interactions

Stephan Block[1,2,*], Srdjan S. Aćimović[1], Nils Odebo Länk[1], Mikael Käll[1,*], Fredrik Höök[1,*]

[1] Department of Physics, Chalmers University of Technology, 412 96 Göteborg, Sweden

[2] Department of Chemistry and Biochemistry, Freie Universität Berlin, Berlin, Germany.

*Corresponding authors: Stephan Block, e-mail: stephan.block@fu-berlin.de; Mikael Käll, e-mail: mikael.kall@chalmers.se; Fredrik Höök, e-mail: fredrik.hook@chalmers.se

Content

Supporting Note S1

Simulation of antenna-enhanced FCS - Antenna-enhanced FCS is a special case of surface-enhanced fluorescence (SEF), which in turn is one of many surface-enhanced spectroscopies (for a comprehensive review, see Fort *et al.*[1]), the most well-known being surface-enhanced Raman scattering (SERS). Far from saturation, in the linear regime, the brightness of a molecule subject to SEF can conveniently be expressed as

$$B \propto \sigma_{\mathrm{a}} I |M_{\mathrm{ex}}|^2 q \,. \tag{S1}$$

Here the first three terms defines the excitation rate, which is set by the absorption cross-section σ_{a}, the excitation intensity I and the intensity enhancement factor $|M_{\mathrm{ex}}|^2$ (M_{ex} being the field-enhancement factor). q is the fluorescence quantum efficiency in the presence of the antenna, which can be written as:

$$q = \frac{k_{\mathrm{rad}}}{k_{\mathrm{rad}} + k_{\mathrm{nr}}^{\mathrm{m}} + k_{\mathrm{nr}}^{\mathrm{i}}} \tag{S2}$$

Here, $k_{\mathrm{rad}} = |M_{\mathrm{em}}|^2 k_{\mathrm{rad}}^0$ is the radiative decay rate, defined by the emission enhancement factor $|M_{\mathrm{em}}|^2$ (related to the radiative photon density of states) and the radiative decay rate of the free molecule, k_{rad}^0. Electromagnetic reciprocity dictates that $|M_{\mathrm{ex}}|^2 \approx |M_{\mathrm{em}}|^2$, that is, the antenna works just as well as a receiver as a receptor, under the assumption that the excitation and emission wavelengths are close and that the incident and emitted waves travel in opposite direction (back-scattering geometry). Eq. (S2) further contains two non-radiative decay rates. $k_{\mathrm{nr}}^{\mathrm{i}}$ quantifies processes that are intrinsic to the molecule and thus not affected by SEF. Together with k_{rad}^0, it defines the quantum efficiency of the free molecule as:

$$q_0 = \frac{k_{\mathrm{rad}}^0}{k_{\mathrm{rad}}^0 + k_{\mathrm{nr}}^{\mathrm{i}}} \,. \tag{S3}$$

$k_{\mathrm{nr}}^{\mathrm{m}}$, on the other hand, takes into account non-radiative decay channels that results in ohmic losses in the metal. It is here convenient to introduce the dissipation enhancement factor:[2]

$$|M_{\mathrm{d}}|^2 = \frac{k_{\mathrm{rad}} + k_{\mathrm{nr}}^{\mathrm{m}}}{k_{\mathrm{rad}}^0} \,. \tag{S4}$$

$|M_{\mathrm{d}}|^2$ (related to the total photon density) of states is only slightly larger than $|M_{\mathrm{em}}|^2$ if the molecule is some distance away from the metal surface. However, very close to

the surface (of the order of a few nm or less), $k_{\mathrm{nr}}^{\mathrm{m}}$ can rapidly increase in magnitude such that $|M_{\mathrm{d}}|^2 >> |M_{\mathrm{em}}|^2$. This can result in complete fluorescence quenching. Combining Eq (S1-S4) yields a net brightness enhancement factor of

$$\frac{B}{B_0} = \frac{|M_{\mathrm{ex}}|^2 |M_{\mathrm{em}}|^2}{(|M_{\mathrm{d}}|^2 - 1)q_0 + 1}. \tag{S5}$$

The net outcome of the different enhancement effects crucially depends on the details of the system considered, including factors like molecular orientation and distance to the metallic antenna, the wavelengths involved and the shape, size, and material properties of the antenna. In particular, Eq. (S5) shows that the intrinsic quantum efficiency is a crucial factor to consider. For example, setting $|M_{\mathrm{ex}}|^2 = |M_{\mathrm{em}}|^2 = |M_{\mathrm{d}}|^2 = |M|^2$ yields a brightness enhancement of $|M|^2$ for a fluorophore in the limit $q_0 = 1$ but $|M|^4$ in the limit $q_0 = 0$, that is, the same scaling as for the SERS enhancement factor. In addition to the brightness enhancement, an antenna can also redirect the angular fluorescence emission pattern and affect the polarization state of the emitted light. Such effects can have large influence on the collection efficiency in an experiment.

We simulated antenna-enhanced FCS using a combination of electrodynamics calculations and Brownian diffusion simulations (**Figure S1**). The spectral response of an isolated silver dimer on glass was simulated using the finite difference time-domain (FDTD) method. Figure S1 shows the scattering cross section in water for a silver dimer with disk radius R = 32 nm, height h = 25 nm and a gap size of 14 nm. The spectra *in air* for this dimer nanoantenna (not shown) are close to the experimental dark field scattering spectra in air (**Figure 1e**, main text). We then calculated the intensity enhancement factor at a surface placed 5 nm away from the substrate and dimer for incident polarization parallel and perpendicular to the dimer axis (**Figure S1b**). This distance corresponds to the expected location of a dye molecule diffusing within the SLB.

The FCS measurement was simulated by performing a 2D diffusive random walk on a surface with a certain intensity enhancement distribution approximating the expected relative fluorophore brightness at any given location. For the bare SLB, we used an intensity distribution with a Gaussian profile with w_0 = 290 nm, thus approximating the laser focus. In the presence of the dimer, the same Gaussian distribution was multiplied by the calculated intensity enhancement distribution. The diffusion coefficient of the random walker was taken as the experimental value of D = 2.3 μm^2/s and the time step in the simulation was taken as Δt = 0.1 μs to be able to resolve the fast component corresponding to the walker entering and leaving the

antenna region. We applied periodic boundary conditions for the random walk with a cell dimension of 2 μm^2.

Figure S1c shows the calculated time traces for the bare surface and the antenna in the two orthogonal polarization directions. The intensity enhancement maps used for this simulation were taken at 561 nm, corresponding to the excitation in FCS experiments. This approximation is validated by the high intrinsic quantum yield of the dye used in the experiments. The data clearly shows pronounced intensity bursts for the antenna-enhanced cases in qualitative agreement with the experimental data. Due to the hotspot, the bursts are higher for parallel than for perpendicular polarization, even though the wavelength considered has much better overlap with the transverse than with the longitudinal plasmon resonance.

We calculated ACFs for the three intensity traces using the correlation function code present in MATLAB (**Figure S1d**). The ACF for the bare SLB was fitted to the one-component model, resulting in τ_D = 5.2 ms. This value was subsequently used to fit ACFs in the presence of the dimer (red lines in **Figure S1d**) using the two-component model given by Eq. (3) in the main text. For longitudinal excitation of the dimer, the fitting procedure resulted in a brightness enhancement factor of E = 76.4 and a fast time component τ_D^* = 15.3 μs. The analysis for transverse excitation yielded E = 33.0 and τ_D^* = 20.8 μs. Performing the same analysis using a dye-surface separation of 10 nm (instead of 5 nm as above) yielded for longitudinal excitation E = 21.0 and τ_D^* = 27.4 μs and for perpendicular excitation E = 8.6 and τ_D^* = 168.4 μs, indicating a strong dependence of the dye-surface separation on the simulation results.

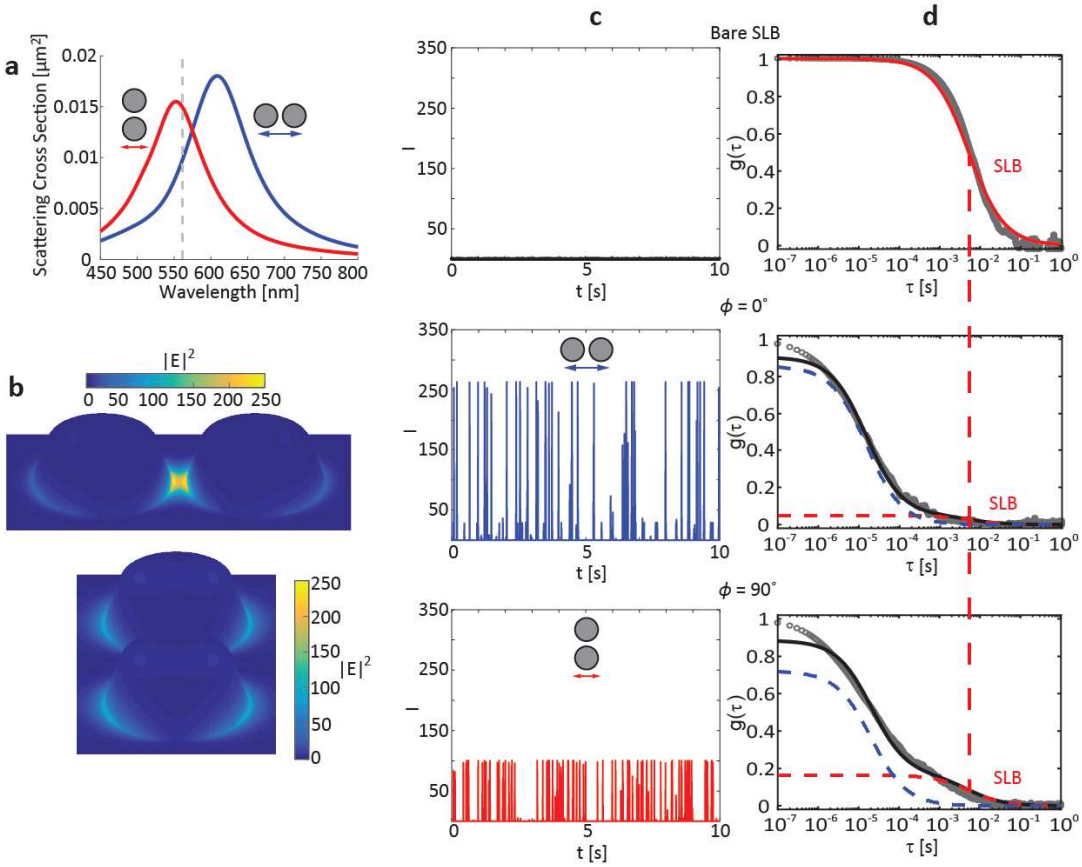

Figure S1: Numerical simulation of antenna-enhanced FCS (**a**) Scattering cross sections of an isolated silver dimer in water. The FCS excitation wavelength, 561 nm, is indicated with a dashed grey line. (**b**) Near-field distributions for excitation at 561 nm for longitudinal excitation, ϕ = 0° (**b, top**), and transverse excitation, ϕ = 90° (**b, bottom**), respectively. The field surface shown is located 5 nm above substrate and dimer, approximately corresponding to the distance to a dye molecule within the SLB. (**c**, **d**) Simulated FCS intensity time traces of a bare SLB (**c, top**) and a SLB-coated silver dimer (**c, middle and bottom**) and the corresponding autocorrelation functions (ACFs, **d**).

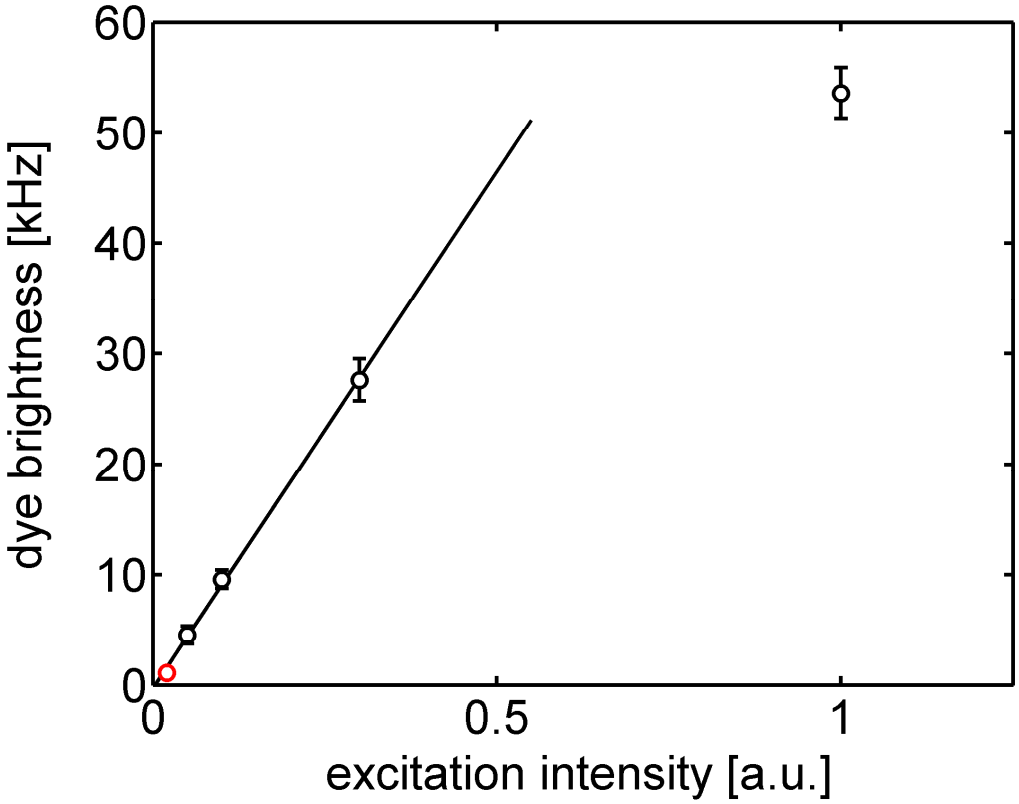

Figure S2: **FCS count rate per dye *versus* excitation intensity.** The average molecular brightness of a single lissamine-rhodamine DOPE lipid within the confocal observation volume (emission interval 570 – 630 nm) increases almost linearly for excitation intensities up to 0.5 % (of the maximum laser power) and saturates at larger intensities at approximately 50 kHz. The red circle indicates the excitation conditions used in the FCS measurements. Error bars indicate standard deviation (see Materials and Methods section for details).

Note S2

Analysis of 2-component autocorrelation functions. The autocorrelation functions (ACFs) of most nanoantennas recorded for longitudinal excitation were not well described using the single component model given by Eq. (1) (main text) since these ACFs contained an obvious short-time decay in addition to the usual component (inflection point around 5 ms) observed far from any antennas. Similar to Punj et al.[3] we fitted all such ACFs using the 2-component model:[4]

$$G(\tau) = 1 + \frac{N\,Q^2 g^0(\tau) + N^* Q^{*2} g^*(\tau)}{\left(N\,Q\ + N^* Q^*\right)^2} \qquad \text{(S6)}$$

containing two single component decay functions, $g^0(\tau)$ and $g^*(\tau)$, defined by:

$$g^0(\tau) = \frac{1}{1+\tau/\tau_{\mathrm{D}}} \text{ and } g^*(\tau) = \frac{1}{1+\tau/\tau_{\mathrm{D}}^*}. \qquad \text{(S7)}$$

This model treats the hotspot as an additional observation volume (indicated by the superscript *) within a background formed by the ordinary confocal observation volume surrounding the nanoantennas. Hence, Q^* (Q) and N^* (N) in Eq. (S6) denote the effective brightness and the absolute number of lipid dyes in the hotspot (background) volumes, respectively.

Under the assumptions that neither the diffusion coefficient nor the surface coverage of the lipid dyes are affected by the presence of a nanoantenna, it is possible to relate N and N^* using the diffusive times by

$$\frac{N^*}{N} = \frac{r_{\mathrm{hs}}^2}{w_0^2} = \frac{\tau_{\mathrm{D}}^*}{\tau_{\mathrm{D}}}. \qquad \text{(S8).}$$

Introducing the effective brightness enhancement factor E through

$$E = Q^*/Q. \qquad \text{(S9)}$$

then allows us to rewrite Eq. (S6) as:

$$G(\tau) = 1 + \frac{1}{N\cdot\left(1+E\tau_{\mathrm{D}}^*/\tau_{\mathrm{D}}\right)^2}\left(g^0(\tau) + E^2\frac{\tau_{\mathrm{D}}^*}{\tau_{\mathrm{D}}}g^*(\tau)\right). \qquad \text{(S10)}$$

This is the fitting function used to analyse all nanoantenna ACFs recorded for longitudinal excitation. It should be noted that all nanoantenna ACF measurements were complemented by measurements in areas lacking nanoantennas on the same sample. This allowed us to specify the lipid diffusion in the SLB in absence of any nanoplamonic structures using the single component model, described by Eq. (1) (main text) and thus to fix the τ_{D} and N values entering Eq. (S10). The fitting process

thus only involves two free parameters, τ_D^* and E (**Figure S3**). These can in turn be translated into lateral hotspot size, r_{hs}, and average dye brightness in the hotspot, Q^*, using the measured confocal radius w_0 and background brightness Q, respectively.

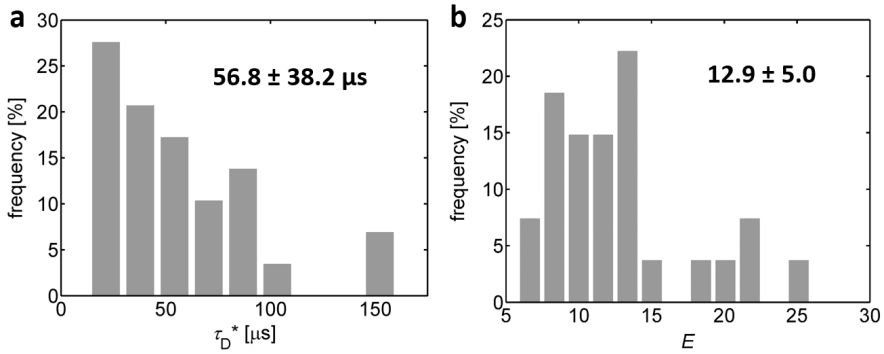

Figure S3: **Distribution of τ_D^* and E among the investigated nanoantennas.** Both, the average hotspot diffusive time τ_D^* (**a**) and enhancement factor (**b**) showed broad distributions, indicative for significant nanoantenna-to-nanoantenna variations. Intervals indicate average value ± standard deviation of the respective parameter, calculated from all investigated nanoantennas.

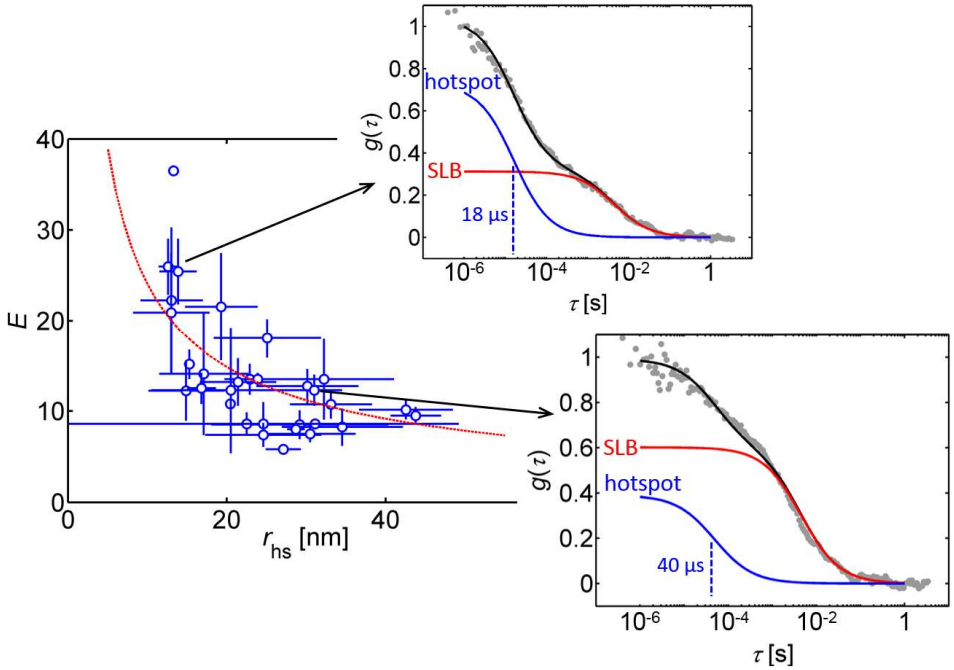

Figure S4: **Correlation of effective hotspot size r_{hs} and average fluorescence enhancement factor E from two-component ACFs for longitudinal excitation.** Two representative ACFs for the case of high and low fluorescence enhancement are shown (the corresponding data points are indicated by black arrows). Intervals indicate average value ± standard deviation derived from measuring at least 6 ACFs per nanoantenna (see Materials and Methods section for details).

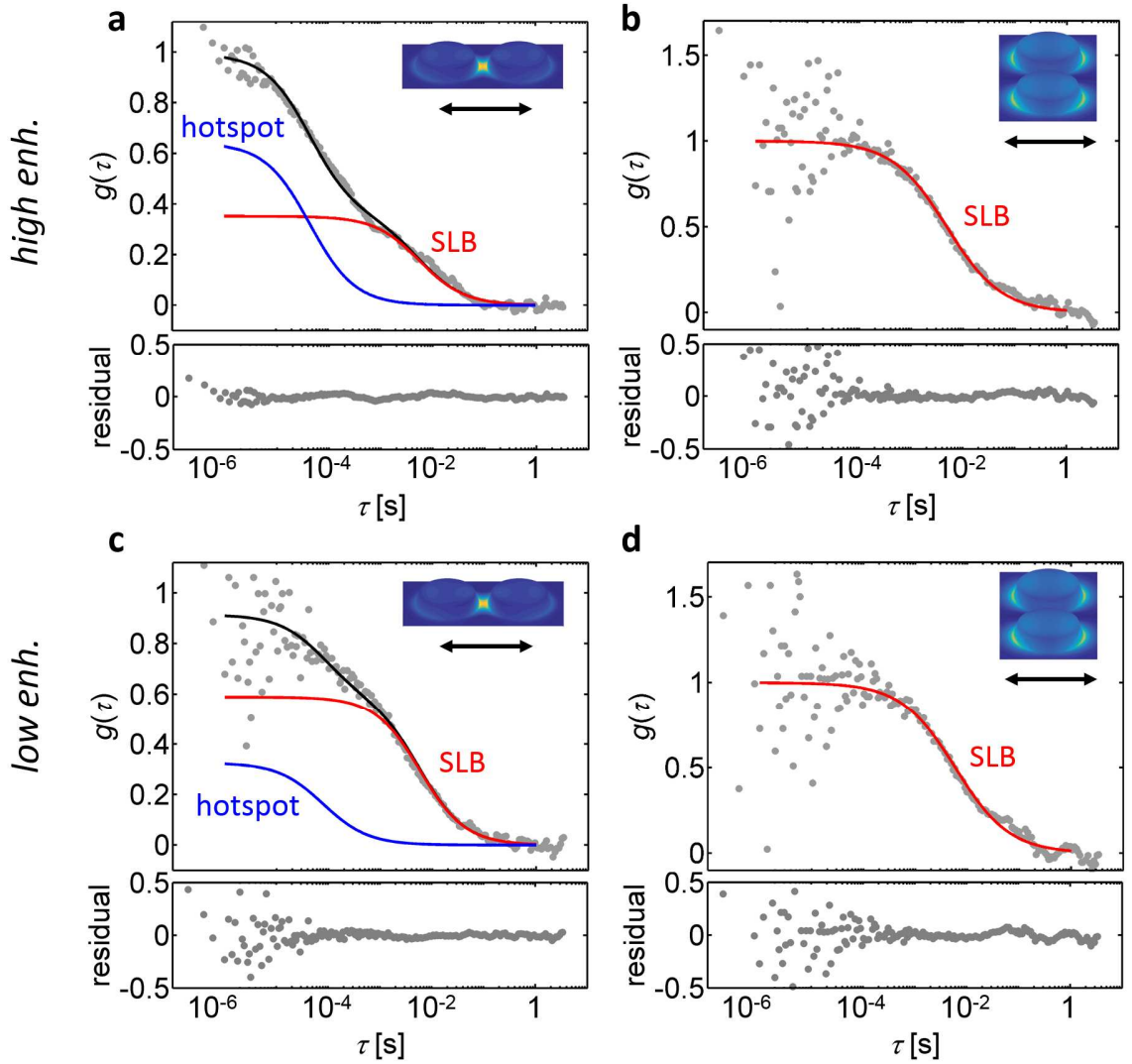

Figure S5: **Representative ACFs from nanoantennas yielding relatively low and high enhancements.** Shown are data from the (**a**, **b**) "high" and (**c**, **d**) "low" enhancement nanoantenna of **Figure 2b** and **2c** (main text), respectively, for longitudinal (**a**, **c**) and transversal (**b**, **d**) excitation. Red lines in (**b**, **d**) are fits to the 1-component model $g^0(\tau)$, but are kept fixed (as described in **Figure S2**), when fitting the 2-component model Eq. (S10) in **a** and **c**. The residuals are given below each ACF.

	SLB	longitudinal excitation		transversal excitation	
	1 comp	*1 comp.*	*2 comp.*	*1 comp.*	*2 comp.*
<*I*> (kHz)	9.2	14.6		10.4	
I_{max} (kHz)	39.0	460		91.0	
$G(0)$-1	*0.14 ± 0.01*	*1.23 ± 0.38*	-	*0.17 ± 0.03*	-
N	7.5 ± 0.7	0.9 ± 0.3	-	5.9 ± 1.1	-
τ_D (ms)	*5.8 ± 1.1*	*1.1 ± 0.9*	**5.8**	*4.5 ± 1.6*	**5.8**
τ_D^* (µs)	-	-	*44.6 ± 12.6*	-	*111 ± 96*
A^*/A	-	-	*1.37 ± 0.33*	-	*0.27 ± 0.09*
r_{hs}	-	-	22.9 ± 3.2	-	33.7 ± 15.7
E	-	-	13.5 ± 1.7	-	4.8 ± 2.8
Q (kHz)	1.2	-	**1.2**	-	**1.2**
Q^* (kHz)	-	-	16.2 ± 2.0	-	5.9 ± 3.4

Table S1: **Parameters extracted from fitting 1- or 2-component ACFs to a "high enhancement" nanoantenna (Figure S5, top).** Given are: average and maximum value of the intensity trace, <*I*> and I_{max}, respectively, the amplitude of the ACF at short lag times, $G(0)$, the corresponding number of dye lipids $N = (G(0)–1)^{-1}$, the diffusive times of the confocal and hotspot volume, τ_D and τ_D^*, respectively, the ratio of the ACF amplitudes of both components at short lag times, A^*/A, the lateral hotspot size, r_{hs}, the average enhancement factor, E, and the average, molecular brightness of a single dye lipid in the confocal and hotspot volume, Q and Q^*, respectively. Italic values indicate results obtained by fitting Eq. (1) or Eq. (S6) to ACFs, while bold values indicate parameters obtained from SLB measurements (control measurements done on the same sample but in areas lacking nanoantennas). Intervals indicate average value ± standard deviation derived from measuring at least 6 ACFs per nanoantenna (see Materials and Methods section for details).

	SLB	longitudinal excitation		transversal excitation	
	1 comp	*1 comp.*	*2 comp.*		*1 comp*
<*I*> (kHz)	9.2	10.8		10.1	
I_{max} (kHz)	39.0	193.0		48.0	
$G(0)$-1	*0.14 ± 0.01*	*0.28 ± 0.09*	-	*0.17 ± 0.02*	-
N	7.5 ± 0.7	3.9 ± 1.3	-	6.1 ± 0.6	-
τ_D (ms)	*5.8 ± 1.1*	*2.4 ± 1.1*	**5.8**	*5.5 ± 1.0*	**5.8**
τ_D^* (µs)	-	-	*52.8 ± 24.2*	-	*604 ± 724*
A^*/A	-	-	*0.63 ± 0.26*	-	*0.13 ± 0.11*
r_{hs}	-	-	24.6 ± 5.8	-	75.6 ± 45.2
E	-	-	8.6 ± 2.4	-	0.9 ± 0.3
Q (kHz)	1.2	-	**1.2**	-	**1.2**
Q^* (kHz)	-	-	10.3 ± 2.9	-	1.1 ± 0.4

Table S2: **Parameters extracted from fitting 1- or 2-component ACFs to a "low enhancement" nanoantenna (Figure S5, bottom).** Given are the same information as in Table S1.

Note S3

Distinguishing hotspot and triplet contributions to the ACF. Triplet dynamics can cause additional components in FCS autocorrelation functions (ACFs) in the range of some µs (**Figure S6a**), which might be confused with a hotspot component. To address this issue, we always performed the FCS measurements (excitation wavelength 561 nm) in 2 readout channels, simultaneously covering the emission ranges of 570 to 630 nm and 630 – 690 nm (see Materials and Methods Section in the main manuscript). We denote these channels as in- and off-resonance channels, respectively, since the nanoplasmonic response of most antennas is located within the wavelength interval covered by the 570-630 nm channel, but not the 630-690 nm channel. Since triplet dynamics cause an additional ACF contribution in both channels (**Figure S6a**), while fluorescence enhancement due to the nanoplasmonic response will be much stronger in the in-resonance channel, and as both channels are simultaneously recorded in the measurements, comparing the ACFs of both channels allows true nanoplasmonic contributions to be distinguished from those due to blinking of the dye (**Figure S6**).

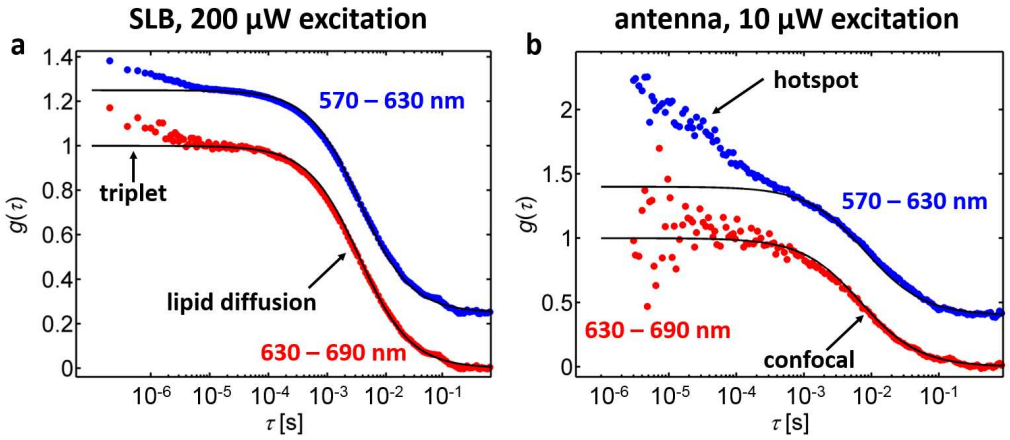

Figure S6: **Comparing in- an off-resonance emission allows triplet and hotspot contributions to be distinguished**. Comparison of fast ACF components (~ few µs) caused by triplet dynamics (**a**) or nanoplasmonic effects (**b**). In (**a**), FCS was performed on a SLB (created on a glass substrate) and the triplet state was excited by operating at relatively high excitation powers. First triplet contributions to the SLB ACF were resolved for excitation powers exceeding 20x the value usually used during the experiments (corresponding to 1 a.u. in Supporting Information Figure S2 or 200 µW total excitation power according to the manufacturer of the microscope). The triplet contribution is resolvable in both readout channels. (**b**) shows a represent-tative nanoantenna-derived two-component ACF (such as those in Figure 2 in the main manuscript), measured at a total excitation power of 10 µW (correspondding to 0.05 a.u. in Supporting Figure 2). The fast ACF component is much more pro-nounced for the readout channel containing the resonance frequency of the nano-antennas (570 – 630 nm) than for the off-resonance channel (630 – 690 nm), which is clearly indicative for a nanoplasmonic origin (*i.e.*, hotspot) of the fast ACF component.

Note S4

Burst analysis and extraction of τ_D^* distributions – For burst analysis,[5-7] the raw data of the FCS experiments had to be processed offline. The raw data stores the time series $\delta T(N)$ of detected fluorescence events in terms of the time that has passed between subsequent events. This means that the first raw data point, $\delta T(1)$, corresponds to the time interval between the first (N = 1) and the second event (N = 2), the second raw data point, $\delta T(2)$, to the interval between the second (N = 2) and third event (N = 3) and so on. For (software-based) calculation of the corresponding FCS autocorrelation function, the raw data was recalculated into an intensity time trace $I(t)$ by counting the number of events occurring between the time interval t and Δt. To allow resolving lag times down to some 10 µs, the intensity time trace was calculated with a temporal resolution/binning of Δt = 1 µs.

As large bursts are equivalent to the observation of many events in a short period of time, *i.e.*, of events having very small $\delta T(N)$, burst can in principle be detected by identifying those events N having much smaller $\delta T(N)$ values than the "background" events created by a SLB. For example, the SLB created in the FCS experiments an average count rate around 9 kHz corresponding to an average δT of SLB-associated events of around 0.11 ms, while hotspot-created bursts led to maximum count rates on the order of few 100 kHz (Table S1) corresponding to average δT values of burst-associated events being much smaller than 10 µs. In order to identify burst-associated events in the FCS data, fluctuations of the $\delta T(N)$ values around their average value were first reduced by smoothing using a moving average filter having a window size of 20 data points and afterwards all those events were identified, whose smoothed δT value fell below a user-defined threshold, which ranged (depending on the enhancement of the particular nanoantenna) between 2.5 and 5 µs, providing sufficient contrast to SLB-associated events. Note that application of the moving average filter to the $\delta T(N)$ data instead of the intensity time trace $I(t)$, which would probably be a more intuitive approach, has the advantage that the average value is taken at constant event density (in contrast to a constant temporal size of the averaging window) reflecting the huge increase in event frequency occurring during bursts. Application of the moving average filter to $I(t)$ would require window sizes being larger than the average δT value to show any effect, therefore leading to window sizes of the order of 1 ms to reduce the noise of SLB-associated events, which would smear out most of the fluctuation details of hotspot-associated events.

For all identified burst events, a cropped version of the entire intensity time trace $I(t)$ was derived, whose window size ranged between 10 and 40 ms (depending on the diffusive time, τ_D*, of the hotspot component as determined from ACFs calculated using the complete intensity time trace $I(t)$ and application of the 2-component fitting

as described in Note S1). It was found that window sizes of 50 – 100 times the τ_D* value of the particular hotspot are large enough to collect a sufficient number of events for calculation the ACF. For all identified burst events, ACFs were calculated from the so derived windows of $I(t)$ and fitted to a 1-component model

$$G(\tau) = 1 + \frac{1}{N^*} \cdot \frac{1}{\left(1 + \tau / \tau_D^*\right)^{\alpha}}, \tag{11}$$

describing a 2D diffusion of (on average) N* dyes through the hotspot having an hotspot diffusive time τ_D*. The parameter α formally indicates the diffusive mode of the dyes (α = 1 for normal diffusion, $\alpha \neq 1$ for anomalous diffusion) and had to be introduced in the fitting procedure, as a large fraction of ACFs led to α values deviating from the expected value of 1 (normal diffusion). It was observed that these burst events (having α values significantly deviating from 1) typically showed a much smaller duration that burst events leading to α values close to one, which indicated that the same dye has to enter and exit the hotspot multiple times to create a proper hotspot ACF and that distortions in the ACF (*i.e.*, $\alpha \neq 1$) are not caused by the presence of anomalous diffusion but by dyes that do not sufficiently often enter and exit the hotspot. This interpretation (*i.e.*, absence of true anomalous diffusion) is supported by the observation that events corresponding to α = 1 and $\alpha \neq 1$ are randomly distributed over the entire intensity time trace $I(t)$, while presence of true anomalous diffusion should cause the observation of only "anomalous diffusion events" over at least a certain period of time. τ_D* histograms as shown in the main text and the Supporting Information were therefore created by regarding only those burst events having an α value ranging between 0.9 and 1.1 (which is the typical range of α values observed for FCS measurements on a bare SLB). Note that this final filtering allows multiple peaks in the τ_D* histograms to be observed (which are hard to resolve without filtering), but does not change the broadness of the τ_D* distribution. This means that the observation of very broad τ_D* histograms in presence of calcium ions (during the FCS measurement) and much narrower τ_D* histograms after EDTA-induced calcium removal is valid also without exclusion of burst events based on their α value.

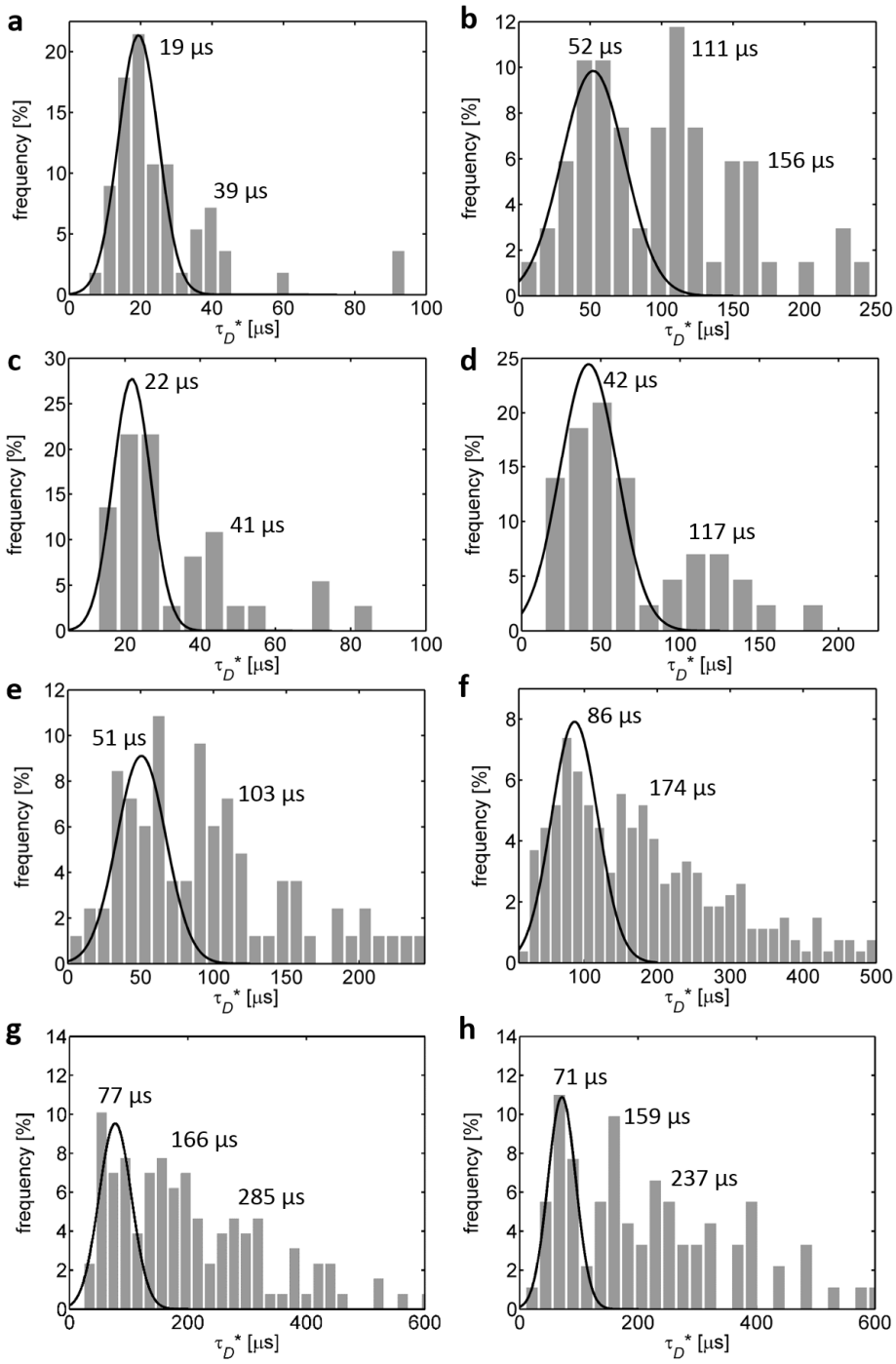

Figure S7: τ_D^* **distributions for various nanoantennas.** For longitudinal excitation, typically broad τ_D^* distributions were observed, showing at least 2 peaks and, in rare cases, hints for a third peak (as indicated in the figure). Although the peak positions varied between different nanoantennas (indicative for differences in the effective hotspot size, r_{hs}), the second peak was observed at twice the τ_D^* value of the first peak. Solid lines are fit to a Gaussian distribution.

Note S5

Burst analysis of fluorescent beads and simulated FCS intensity traces – Although the EDTA-induced removal of calcium ions indicate that the broad τ_D* histograms observed in presence of calcium ions cannot be an analysis artefact (**Figure 4**, main text), we sought for another controls to validate the analysis concept. This was done (*i*) by analysing FCS measurements involving fluorescent beads and (ii) by analysing simulated FCS intensity traces (derived as detailed in **Note S1**).

We first measured FCS using a diluted sample of TetraSpeck beads (Life Technologies, Darmstadt, Germany) diffusing through bulk, which are bright enough to achieve a similar brightness contrast to the background as rhodamine-dyes that diffuse through a hotspot. The TetraSpeck sample was diluted so that most of the intensity time trace $I(t)$ was generated by "background" events originating from the solution, while occationally a single TetraSpeck bead diffused through the confocal field of view, creating large bursts in $I(t)$. The diffusive time, τ_D, of TetraSpeck beads was on the order of 2.5 ms, suggesting to employ a window size of 500 ms in the data analysis (instead of the few 10 ms used for hotspot-associated bursts). Since the TetraSpeck beads showed similar burst count rates as the nanoantenna sample, a similar δT threshold (5 – 10 µs) was used to identify bursts events. This finally yielded τ_D distributions that showed only a single peak (**Figure S8**), which was closely located to the τ_D value observed using the common FCS analysis.

Additionally, simulated FCS intensity traces (generated as described in **Note S1**) were subjected to the same burst analysis that was also applied to antenna-enhanced FCS data, allowing to compare the hotspot component extracted using the entire FCS intensity trace (**Figure S9a**) or short intervals thereof (**Figure S9b**). Again, only a single peak is observed in the τ_D^* distribution, exhibiting a peak τ_D^* value being close to the average diffusive time of the hotspot component that was derived from the 2-component fit, Eq. (S10).

These findings prove, in addition to the EDTA-based control measurement, that the observation of multiple peaks is not caused by the burst analysis but indicative for distinct lipid sub-populations differing in their diffusive times.

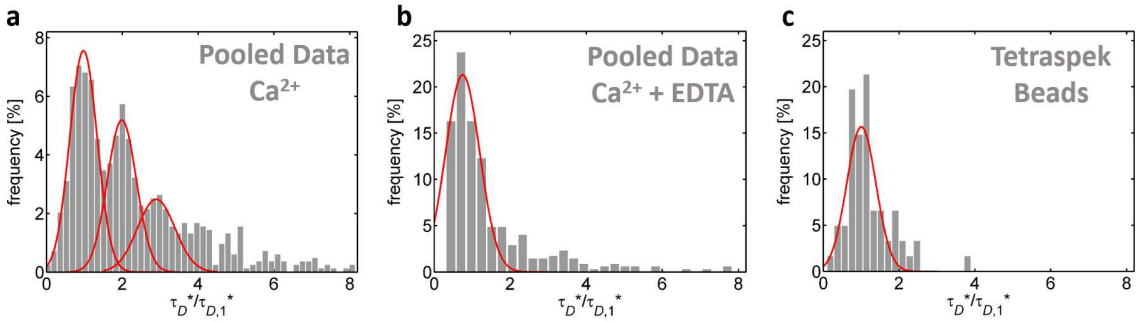

Figure S8: **Comparison of diffusive time distributions recorded for nanoantennas and fluorescent beads.** Shown are pooled τ_D^* distributions originating from nanoantenna experiments (**a**, **b**) and a representative τ_D distribution from an analysis of intensity bursts created by bright, fluorescent beads entering the confocal volume (**c**; see text for detail). The lack of multiple peaks in **c** clearly indicated that the peak structure observed in the nanoantenna measurements (**a**) is not an artifact of the burst analysis. Further, removal of calcium ions by EDTA caused a τ_D^* distribution (**b**) that was also dominated by a single peak. In addition, the single peaks in **a** and **b** had a similar width as the one in **c**, indicating that the peak width mainly reflects the measurement uncertainty connected to the determination of the corresponding diffusive time.

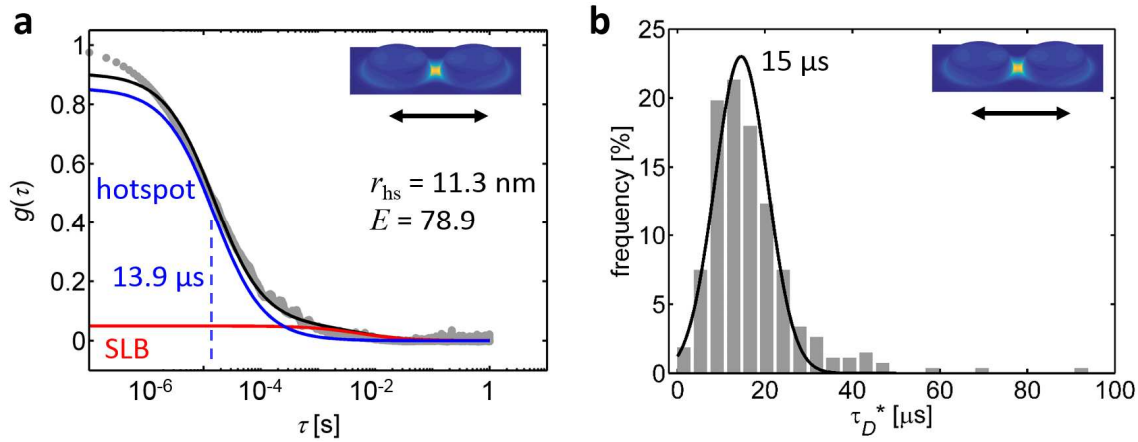

Figure S9: **Burst analysis of simulated FCS intensity traces.** FCS measurements were simulated as detailed in **Note S1** and the same burst analysis was applied as used for the experimental, antenna-enhanced FCS measurements. In the simulation, only a single lipid species diffusing with 2.3 $\mu m^2/s$ was present. (**a**) In agreement with the experiments, the ACF (of the entire intensity trace) showed a SLB- and hotspot component. (**b**) The burst analysis extractred a single-peaked τ_D^* distribution with a peak position in good agreement with the 2-component analysis (**b**).

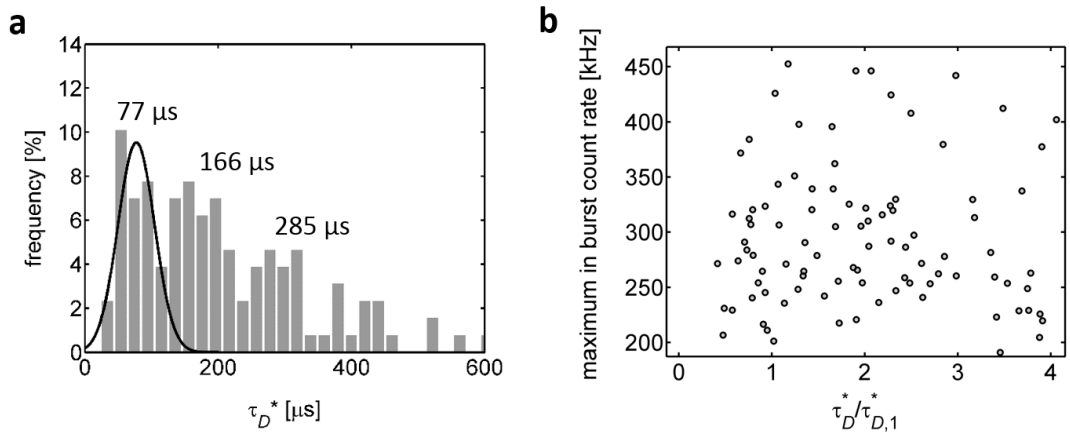

Figure S10: **Lipid-lipid complexes contain only a single dye-labeled lipid.** Comparison of (**a**) the τ_D^* distribution of a representative nanoantenna (also shown in Supporting Information Figure S6g) and (**b**) the corresponding correlation of τ_D^* values and maximum burst count rates for each burst contributing to the histogram in (**a**). There is no correlation between τ_D^* and the maximum count rate, indicating that Ca^{2+}-mediated lipid-lipid complexes contain only a single dye-labeled lipid (in agreement with theoretical considerations according to the low molar fraction of dye-labeled lipids within the SLB).

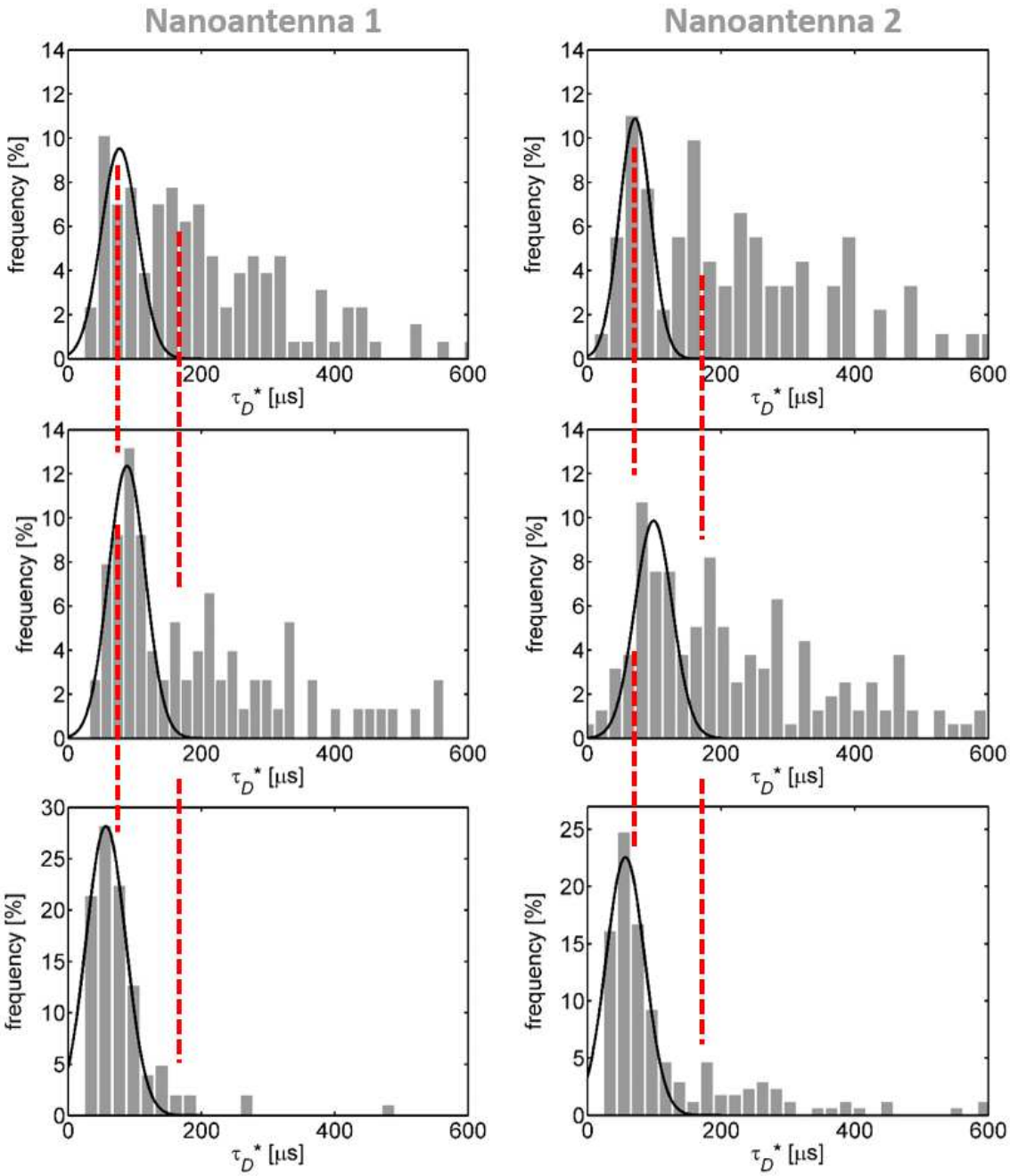

Figure S11: **Temporal evolution of τ_D^* distributions after EDTA addition**. Shown are τ_D^* distributions for 2 nanoantennas (**left** and **right**, respectively) recorded prior to EDTA addition (**top row**), 20 min (**middle row**), and 60 min (**bottom row**) after addition of 10 mM EDTA to the bulk.

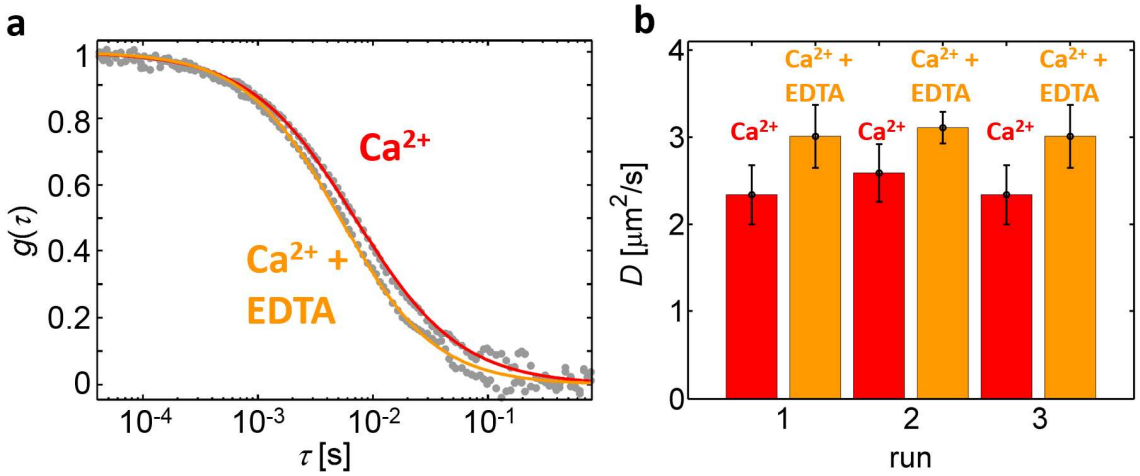

Figure S12: **Addition of EDTA increases lipid mobility in confocal FCS experiments**. Hints for lipid-lipid complex break up are resolvable even when using (ensemble-averaging) confocal FCS by comparing ACFs (**a**) obtained from SLBs in presence of calcium ions (5 mM Ca^{2+} dissolved in a Tris-HCl buffer; **red**) with those obtained after calcium ion removal (addition of 10 mM EDTA; **orange**). **Grey dots** indicate the experimentally derived ACFs (after normalization using $g(\tau)=[G(\tau)-1]/[G(0)-1]$), while **solid lines** are fits to Equation (1). Typically, an increase in lipid mobility is observed after EDTA addition, indicated by a decrease in the diffusive time (**a**), which can be translated into an increase in (ensemble-averaged) lipid diffusive coefficient from (2.47 ± 0.13) $\mu m^2/s$ to (3.06 ± 0.05) $\mu m^2/s$ (average ± standard deviation of the diffusive coefficients determined from 3 independent measurements recorded using 3 independent samples as shown in **b**; $p < 0.01$ using an unpaired *t* test).

REFERENCES

(1) Fort, E.; Gresillon, S. Surface Enhanced Fluorescence. *J. Phys. D: Appl. Phys.* **2008**, *41*, 013001.

(2) Johansson, P.; Xu, H. X.; Kall, M. Surface-Enhanced Raman Scattering and Fluorescence near Metal Nanoparticles. *Phys. Rev. B* **2005**, *72*, 035427.

(3) Punj, D.; Mivelle, M.; Moparthi, S. B.; van Zanten, T. S.; Rigneault, H.; van Hulst, N. F.; Garcia-Parajo, M. F.; Wenger, J. A Plasmonic 'antenna-in-box' Platform for Enhanced Single-Molecule Analysis at Micromolar Concentrations. *Nat. Nanotechnol.* **2013**, *8*, 512-516.

(4) Zander, C.; Enderlein, J.; Keller, R. A. *Single Molecule Detection in Solution: Methods and Applications,* 1st ed.; Wiley-VCH: Berlin, 2002.

(5) Eggeling, C.; Fries, J. R.; Brand, L.; Gunther, R.; Seidel, C. A. M. Monitoring Conformational Dynamics of a Single Molecule by Selective Fluorescence Spectroscopy. *Proc. Natl. Acad. Sci. U. S. A.* **1998**, *95*, 1556-1561.

(6) Eggeling, C.; Berger, S.; Brand, L.; Fries, J. R.; Schaffer, J.; Volkmer, A.; Seidel, C. A. M. Data Registration and Selective Single-Molecule Analysis Using Multi-Parameter Fluorescence Detection. *J. Biotechnol.* **2001**, *86*, 163-180.

(7) Zhang, K.; Yang, H. Photon-by-Photon Determination of Emission Bursts from Diffusing Single Chromophores. *J. Phys. Chem. B* **2005**, *109*, 21930-21937.